

Ambipolar charge transfer of larger fullerenes enabled by the modulated surface potential of h-BN/Rh(111)

Max Bommert, Bruno Schuler, Carlo A. Pignedoli, Roland Widmer, Oliver Gröning*

Empa, Swiss Federal Laboratories for Materials Science and Technology, nanotech@surfaces Laboratory, 8600, Dübendorf, Switzerland

ARTICLE INFO

Keywords:

Fullerenes
2D materials
Ambipolar charge transfer
Intermolecular interactions
Organic hybrid electronics
Scanning tunneling microscopy
Non-contact atomic force microscopy

ABSTRACT

A detailed understanding of how molecules interact with two-dimensional materials, particularly concerning energy level alignment and charge transfer processes, is essential to incorporate functional molecular films into next-generation 2D material-organic hybrid devices. One of the major challenges in integrating molecular films in field-effect transistors is facilitating ambipolar charge transport, which is often hindered by the large electronic gap of the organic layers. This work compares the adsorption site-dependent energy level alignment of C₆₀, C₇₀, and C₈₄ fullerenes induced by the spatial variation of the electrostatic surface potential of the h-BN/Rh(111) Moiré superstructure. As the size of the fullerenes increases, the HOMO-LUMO gap shrinks. In the case of C₈₄, we find an intrinsic charge transfer from the substrate to the fullerenes adsorbed in the Moiré pore centers, rendering them negatively charged. The electric field effect-induced charging of neutral fullerenes and discharging of intrinsically negatively charged fullerenes are investigated using scanning tunneling spectroscopy, non-contact atomic force microscopy, and Kelvin probe force spectroscopy. Our findings show that on metal-supported h-BN, the LUMO level of C₈₄ is sufficiently close to the Fermi energy that it can be neutral or 1e⁻ negatively charged depending on slight variations of the electrostatic potential. The findings propose a path to make ambipolar charge transfer accessible and efficient by circumventing the need to overcome the fullerenes' electronic gap.

1. Introduction

Over the past decade, there has been growing interest in combining functional organic molecules with inorganic two-dimensional (2D) van der Waals (vdW) materials to create organic/inorganic heterojunctions. With the aim of miniaturizing and optimizing devices, the combination of these two material classes has been successfully implemented in electronic [1,2] and optoelectronic devices [3], solar cells [1], memory devices [4], and energy storage applications [5]. A shared prerequisite for designing and optimizing these applications is a detailed understanding of how the molecules interact electronically with each other and with the 2D materials.

One particular area of focus has been the integration of molecular layers as active channels in field-effect transistors (FETs). The advantages of organic semiconductors in versatility, tailored synthesis, and scalability have been shown to enhance the performance of existing 2D devices and pioneer new device architectures for flexible and transparent electronics [6,7]. Among the molecules suitable for application in FETs, the family of fullerenes has emerged as a promising candidate for

n-type transport due to their high electron affinity and decent electron mobility [8–10]. While unipolar FETs have advanced rapidly in terms of single-channel transport properties, the implementation of molecules for ambipolar charge transport has proven challenging. Device performance is limited by multiple factors, such as the typically large gaps between the highest occupied molecular orbital (HOMO) and the lowest unoccupied molecular orbital (LUMO), where the HOMO is used to inject holes and the LUMO to inject electrons. Additionally, the energy level alignment of the molecules needs to be finely tuned to avoid an imbalance in the electron/hole charge carrier densities [11].

Previous research has shown promising results in overcoming the challenges to achieve ambipolar charge transport in fullerenes by designing fullerene derivatives [12,13], synthesizing metallofullerene peapods to reduce the HOMO-LUMO gap [14], or introducing co-crystals that contain organic donors and acceptors [15]. However, these approaches significantly increase the complexity of the devices.

This work proposes a way to achieve ambipolar charge transfer in larger fullerenes without the need for additional chemical modifications on the molecules by carefully selecting the molecule-2D material

* Corresponding author.

E-mail address: oliver.groening@empa.ch (O. Gröning).

<https://doi.org/10.1016/j.carbon.2023.118592>

Received 12 September 2023; Received in revised form 26 October 2023; Accepted 2 November 2023

Available online 3 November 2023

0008-6223/© 2023 The Authors. Published by Elsevier Ltd. This is an open access article under the CC BY license (<http://creativecommons.org/licenses/by/4.0/>).

combination. Among the plethora of 2D materials investigated today, hexagonal boron nitride (h-BN) has proven highly useful for devices as a substrate [16] and gate insulator [17] due to its large electronic bandgap and lack of states near the Fermi energy. It has also served as a platform for investigating molecules with scanning probe techniques, effectively decoupling molecules electronically from underlying metal substrates [18,19]. We recently demonstrated the possibility of using the spatial variations of the electrostatic surface potential of the h-BN/Rh(111) Moiré superstructure to tune the energy level alignment of the C₆₀ fullerene [20]. Here, we use low-temperature scanning tunneling spectroscopy (STS) to compare the energy level alignment and charge transfer processes of three fullerenes, C₆₀, C₇₀, and C₈₄, on the h-BN/Rh(111) Moiré superstructure. As the fullerene size increases, the band gap of the fullerenes shrinks significantly [21]. Based on this effect, we explore the possibility of intrinsically doping part of the fullerenes via charge transfer from the substrate and charging/discharging via the field effect with a combination of non-contact atomic force microscopy (nc-AFM) and Kelvin probe force spectroscopy (KPFs). The proposed approach facilitates ambipolar, i.e., fullerene-to-substrate and substrate-to-fullerene electron transfer, using the same molecular orbital occupied or unoccupied as both an electron donor and acceptor.

2. Results and discussion

2.1. Adsorption configuration

Fig. 1 (a)–(c) presents schematic ball-stick models of the C₆₀, C₇₀, and C₈₄ fullerenes used in the experiments. The C₈₄ material consists of a mixture of the two isomers D₂ and D_{2d} with a ratio of about 2:1. In the first step of sample preparation, a single layer of h-BN was epitaxially grown under UHV conditions on Rh(111) single crystals via thermal decomposition of Borazine gas, resulting in the formation of the h-BN/Rh(111) Moiré superstructure. This structure is characterized by a hexagonal arrangement of so-called pore and wire regions with 3.2 nm periodicity [22]. Subsequently, the fullerenes were sublimated onto the h-BN/Rh(111) substrates. The h-BN/Rh(111) substrate was heated to

approximately 100 °C during sublimation to promote molecular island formation.

We find that all three fullerene types have a strong tendency to form molecular clusters of at least seven molecules in the pores of the Moiré, and the corresponding STM topographic images are shown in Fig. 1 (d)–(f). Only for the C₈₄, we rarely find individual fullerenes not incorporated in heptamer clusters or larger islands. The structure of extended fullerene islands for C₆₀, C₇₀, and C₈₄ are shown in Fig. 1 (g)–(i), respectively. From the intermolecular contrast of the STM topographies, we can conclude that in all three cases, the rotational adsorption configuration of the individual molecules in the islands is uncorrelated and appears random.

For C₆₀ islands, there is a near-perfect commensurability between the fullerene lattice and the underlying superstructure of the h-BN/Rh(111) Moiré. With regard to the C₆₀ layer, the Moiré results in a commensurate $2\sqrt{3} \times 2\sqrt{3}$ R30° superstructure with the same periodicity as the h-BN/Rh(111) superstructure of 3.2 nm (see SI Figure S1). With respect to the underlying substrate it can be described as a $(2\sqrt{3} \times 2\sqrt{3})$ a_{C60}/(13 × 13) a_{hBN}/(12 × 12) a_{Rh} coincidence lattice, with the respective lattice parameters of a_{C60} = 0.95 nm, a_{hBN} = 0.25 nm and a_{Rh} = 0.27 nm [20, 23].

In the case of smaller C₇₀ islands, we can still observe a contrast in the apparent height for some of the wire regions. With a mean distance of 0.99 ± 0.04 nm between C₇₀ we find a lattice mismatch of 7 % compared to the h-BN/Rh(111) Moiré superstructure. For C₈₄, the apparent height modulation is completely lost, and no regularity is present in the apparent height of the molecular lattice. The loss of the apparent height modulation for C₇₀ and C₈₄ can be explained by a loss of commensurability between the superstructure and the molecular lattices as the size of the fullerenes increases. All the fullerenes assemble in a triangular lattice. While the lattice vectors of the larger C₆₀ islands align with the high symmetry directions of the Moiré, this is not necessarily the case for the C₈₄ islands. A more detailed analysis is presented in the supplementary material Figure S2.

Despite achieving intermolecular contrast for C₈₄, distinguishing between the two isomers D₂ and D_{2d} via STM is not possible due to the

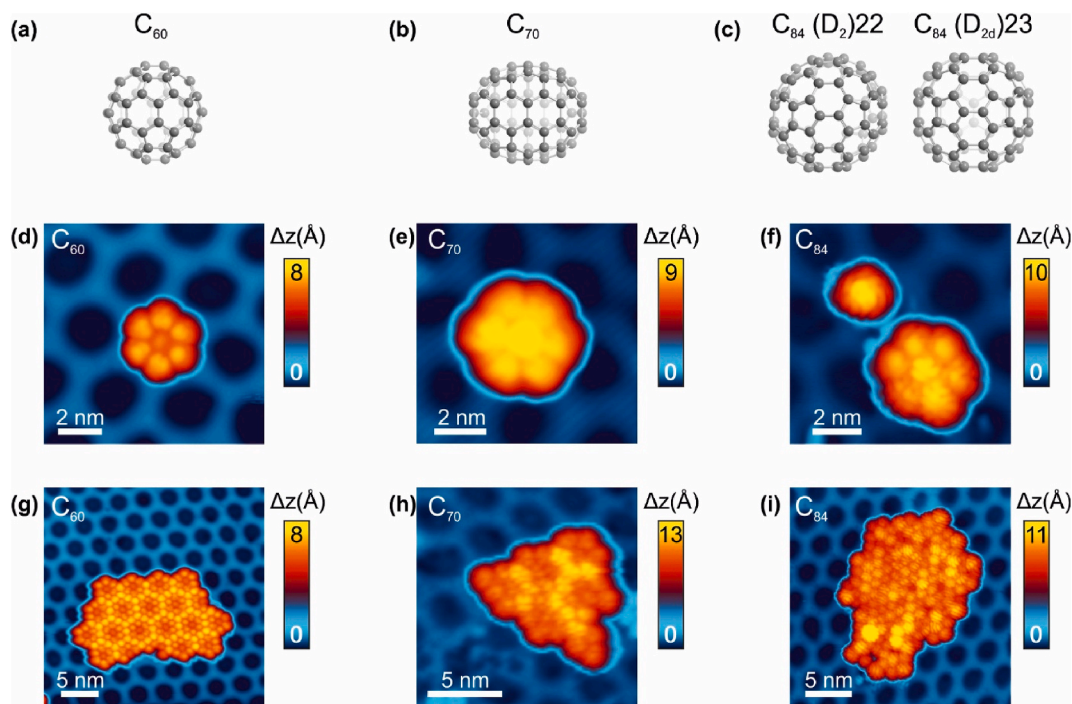


Fig. 1. STM topographies of the studied fullerenes on h-BN/Rh(111). Ball-stick models of (a) C₆₀, (b) C₇₀ and (c) the two C₈₄ isomers D₂ and D_{2d}. STM topographies of small fullerene clusters (d) C₆₀ (setpoint: −0.5 V, 20 pA), (e) C₇₀ (setpoint: 1 V, 10 pA) and (f) C₈₄ (setpoint: 1 V, 10 pA). STM topographies of fullerene islands (g) C₆₀ (setpoint: −1 V, 10 pA), (h) C₇₀ (setpoint: 1 V, 10 pA) and (i) C₈₄ (setpoint: −1.2 V, 10 pA).

rotational disorder and the complex orbital structure in the inhomogeneous surface potential variation of the h-BN/Rh(111) superstructure [24].

2.2. Electronic characterization

Electrochemistry experiments [21] and electron-energy-loss spectroscopy [25] have shown that one can expect a decrease in the fullerenes' HOMO-LUMO gap for increasing fullerene size. As the number of carbon atoms increases, the electronic shell of the fullerenes approaches the one of graphene. Furthermore, while for C_{60} , all atoms are geometrically equivalent, this is not necessarily true for larger fullerenes. The result is that symmetry decreases due to different isomeric forms, and thus, the degeneracy of the molecular orbitals can be lifted. Consequently, the frontier orbital structure at the Fermi energy becomes wider and the HOMO-LUMO gap shrinks.

A comparison of DFT calculations found in literature for the HOMO-LUMO gaps of C_{60} , C_{70} [26], and C_{84} [27] is shown in Fig. 2 (a). All calculations presented were performed with the B3LYP functional, which has shown a good agreement with experimentally obtained HOMO-LUMO gaps of fullerenes [26]. From the calculations, we can expect a moderate reduction of the gap by 2.5 % for C_{70} and a more substantial 28 % (D_2) to 26 % (D_{2d}) for the C_{84} isomers compared to C_{60} . The two isomers of C_{84} have comparable HOMO-LUMO gaps. However,

the HOMO and LUMO of the D_{2d} isomer are both two-fold degenerate, whereas for the D_2 isomer, this degeneracy is lifted, and HOMO and LUMO are non-degenerate, however, with only minor energy differences to the HOMO-1 and LUMO+1 respectively.

We characterized the energy position of the frontier orbitals for all three fullerenes via STS and found three different scenarios depending on the relative adsorption position of the fullerene with respect to the h-BN/Rh(111) superstructure. An influence of the adsorption position on the level alignment of the frontier orbitals can be expected due to the periodic modulation of the surface potential, which originates from the closely bound B and N atoms in the pore region being subject to polarization effects induced by the interaction with the metal. The modulation is characterized by a surface potential difference of about 0.5 V between the superstructure's pore (with a work function of 3.6 eV) and wire (4.1 eV) regions [24].

Fig. 2 (b) shows dI/dV spectra for neutral fullerenes adsorbed on top of the wire section of the h-BN/Rh(111) superstructure, which is characterized by a relatively high work function, i.e., a large electrostatic surface potential. For all three fullerene types, we find the characteristic signature of the LUMO orbital in the positive sample bias range with no features around Fermi energy and a shoulder emerging for negative sample bias, which we can identify as the onset of the HOMO. The STS measurements allow us to determine the HOMO-LUMO gaps for $C_{60} = 3.1 \pm 0.2$ eV, $C_{70} = 3.0 \pm 0.2$ eV, and $C_{84} = 2.3 \pm 0.2$ eV. The measured

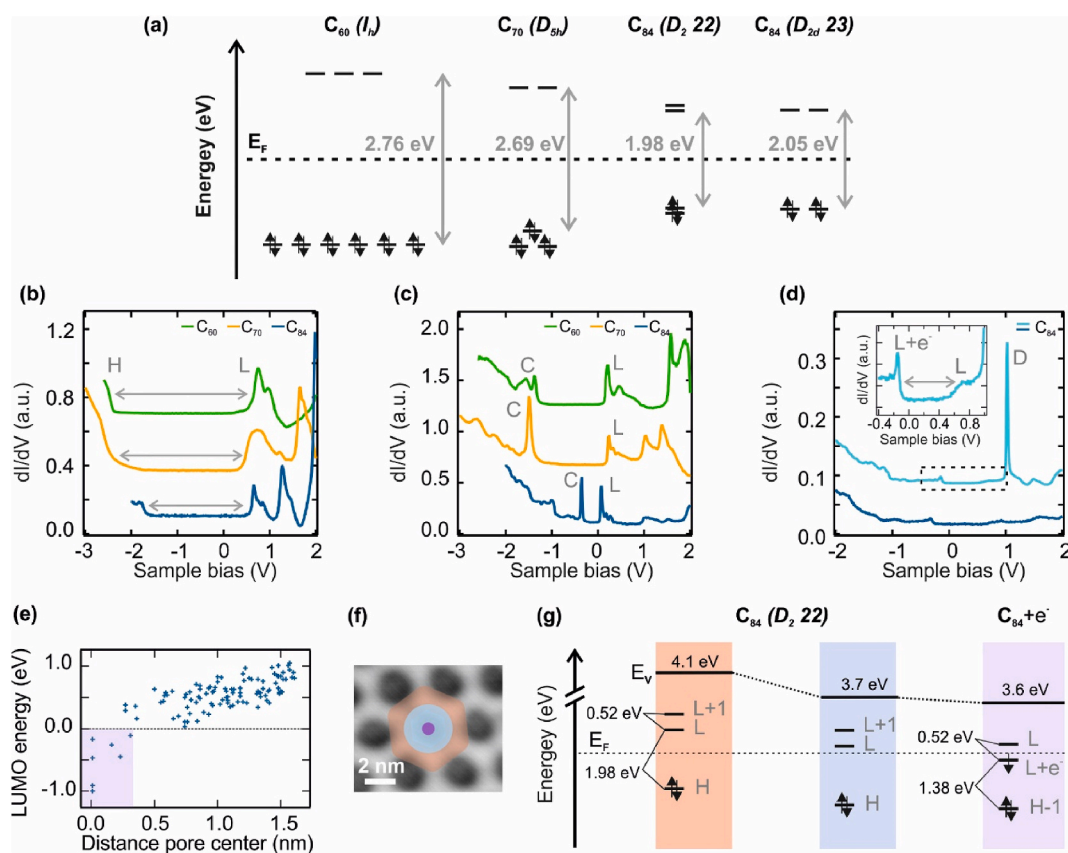


Fig. 2. Electronic characterization of the fullerenes. (a) DFT calculations of the HOMO-LUMO gap with B3LYP functional for the frontier orbitals taken from literature for C_{60} , C_{70} [26] and C_{84} [27]. (b) STS spectra for C_{60} green (setpoint: 1.25 V, 750 pA), C_{70} yellow (setpoint: 1.25 V, 750 pA) and C_{84} blue (setpoint: 2 V, 200 pA) adsorbed on the wire of the Moiré superstructure. HOMO and LUMO labeled H and L and HOMO-LUMO gaps indicated with grey arrows. (c) STS spectra for C_{60} green (setpoint: 1.25 V, 750 pA), C_{70} yellow (setpoint: 1.25 V, 750 pA) and C_{84} blue (setpoint: 2 V, 200 pA) adsorbed in the pore of the Moiré superstructure. LUMO labeled L and charging peak labeled C. (d) STS spectra of C_{84} adsorbed in the pore center (setpoint: 2 V, 200 pA). The light blue spectra shows a discharging peak labeled D. The inset shows the former LUMO that is now populated labeled $L + e^-$ and the new LUMO orbital. The $L + e^-$ and L gap is indicated. (e) LUMO energy vs. Distance to pore center for 108 measured C_{84} . C_{84} showing the $L + e^-$ feature in the negative bias range are highlighted in violet. (f) STM topography of h-BN/Rh(111) Moiré superstructure with the wire (red), pore (blue) and pore center (violet) regions color-coded (setpoint: -0.5 V, 10 pA). (g) DFT calculated energy level diagram for C_{84} (red and blue) and $C_{84}+e^-$ (violet). HOMO and LUMO indicated with H and L respectively. For C_{84} there is an intrinsic charge transfer from the substrate to the fullerenes (violet) adsorbed in the pore center.

HOMO-LUMO gaps are slightly larger than the values suggested by DFT. However, the relative HOMO-LUMO gap reduction of 3.3 % between C_{70} and C_{60} seen in the experiment is in good agreement with the DFT calculations. For C_{84} , the HOMO-LUMO gap is reduced more significantly. The measured reduction is 26 % and is in excellent agreement with the predicted values of the DFT calculations.

We also find that the HOMO-LUMO gap is asymmetric, with the LUMO significantly closer to the Fermi level than the HOMO. This can be rationalized by the vacuum level alignment of the C_{60} when the fullerene comes in contact with the substrate. Due to the sizable HOMO-LUMO gap of the C_{60} and its larger work function (4.7 eV) [28] as compared to the of the h-BN/Rh(111) (4.1 eV wire region) [24], the mid gap energy of the C_{60} will be below the Rh(111) Fermi level and the LUMO accordingly closer to the Fermi Energy as the HOMO. A schematic energy level diagram is shown in Figure S3.

The energy level alignment changes for fullerenes adsorbed closer to the pore. The LUMO approaches the Fermi energy further as the adsorption position of the molecule approaches the pore center, as seen in Fig. 2 (c). This change in energy level alignment is due to the variation of the surface potential on the h-BN/Rh(111), which has its minimum in the pore center and is, as indicated before, about 0.5 V lower than on the wire regions [24].

Consistent with the effects of energy level alignment on inter-fullerene hybridization, the LUMO orbital of molecules close to or in the center of a pore has a smaller FWHM by a factor of up to 5. This sharpening of the orbital features has been observed before for C_{60} in the pore centers of h-BN/Rh(111) and is due to the electronic decoupling of these molecules from their neighbors. Here, we can now corroborate this effect also for C_{70} and C_{84} [20]. In addition to the LUMO shifting closer to the Fermi energy, we find a new sharp feature emerging in the dI/dV spectra at negative sample bias. This new feature is observed for fullerenes when the LUMO energy position is less than 0.3 eV from the Fermi energy. The additional feature, labeled C in Fig. 2 (c), is attributed to a charging peak corresponding to adding one electron in the LUMO. Due to the decoupling properties of the h-BN, the STM-tip fullerene substrate system can be seen as a double barrier-tunneling junction. The electron transfer occurs when the electric field of the STM tip is large enough to shift the LUMO below the Fermi energy, which leads to the opening of an additional electron tunneling channel and the characteristic charging peak in the dI/dV spectra [19]. Notably, in Fig. 2 (c), the C_{84} charging peak occurs at the smallest negative bias, i.e., only a small electric field is needed to shift the LUMO below Fermi energy. The voltage V_C at which the charging occurs depends linearly on the LUMO position V_{LUMO} via $-a \cdot eV_C = eV_{LUMO}$ [19]. Here, the parameter a denotes the capacitive coupling of the STM bias voltage to the C_{84} energy levels and is determined by the voltage drop across the dielectric h-BN. Accordingly, the LUMO is lowered in energy by $\Delta E = a \cdot eV_{Bias}$ as a function of the applied sample bias V_{Bias} . Once V_{Bias} reaches the critical voltage V_C to charge the fullerene, the LUMO aligns with the Fermi energy and is transiently populated with an electron. From the measured ratio of V_{LUMO}/V_C we find $a=0.162 \pm 0.025$.

In the case of the C_{84} , we find a third scenario with a fundamentally different dI/dV signature, shown in Fig. 2 (d). In 6 % of 109 measured C_{84} , the dI/dV spectra lack the characteristic LUMO signature in the positive sample bias range. Instead, a new feature appears in the negative sample bias range labeled L + e^- . This observation points to a newly occupied state near the Fermi energy. In analogy to the STM tip-induced field effect charging discussed earlier, we find a sharp feature in the positive sample bias range if L + e^- is close (<0.3 eV) to Fermi energy.

Because of the lack of commensurability between the C_{84} lattice and the h-BN superstructure, the exact adsorption position of the individual molecules with respect to the superstructure is difficult to determine directly from the apparent height in the STM topographies. To investigate the effect of the adsorption position on the energy level alignment, we extrapolated the Moiré pore centers from the surrounding uncovered substrate into the molecular islands. In Fig. 2 (e), the LUMO position is

plotted against the extrapolated distance of the C_{84} to the pore center. We find a clear trend of LUMO shifting towards Fermi energy the closer the C_{84} is adsorbed to the pore center. For C_{84} molecules adsorbed within less than 0.4 nm from the pore center, we find no LUMO signature in the positive sample bias range but consistently find the new L + e^- feature in the negative bias range. From this, we conclude that due to the small HOMO-LUMO gap and the gating effect of the Moiré superstructure, 6 % of the C_{84} are intrinsically charged by the substrate. The newly occupied state L + e^- is a formerly unoccupied LUMO orbital. The now-occupied molecular orbital can be discharged via the field effect of the STM tip at positive biases, which gives rise to the peak labeled D in Fig. 2 (d).

It is noteworthy that the spread of the LUMO positions is between -1 and 1 V, whereas the electrostatic potential of the h-BN/Rh(111) Moiré ranges only from 0 to 0.5 V. The large spread of the LUMO energies in the positive bias range can be attributed to the lack of symmetry in the C_{84} and the lifting of degeneracies in the orbitals. Subsequently, the adsorption orientation can significantly influence the LUMO position. Additionally, intermolecular Coulomb interactions of the charged C_{84} can influence the energy level alignment, which will be discussed later. Concerning the LUMO positions in the negative bias range, one can expect a jump in the energy level alignment upon charge transfer.

DFT calculations of the HOMO-LUMO gap for the three adsorption positions color-coded in Fig. 2 (f) are presented in Fig. 2 (g). The DFT calculations are for the neutral and negatively charged C_{84} D₂ isomer in vacuum, and the energy level alignment was chosen to match the experimental data. The difference in the work function of the Moiré superstructure between wire (4.1 eV) and pore (3.6 eV) appears nearly step-like [18]. Only C_{84} adsorbed in the center of the pores are subject to charge transfer. The DFT calculations for the charged C_{84} predict a significant reduction in the HOMO-LUMO gap by 81 %. The measured HOMO-LUMO gap of the charged C_{84} , as shown in Fig. 2 (d), is 0.76 eV, which equals a reduction of 76 % and agrees well with the DFT calculations. Additional information on the DFT calculations for charged and neutral C_{84} for both D₂ and D_{2d} isomers is provided in the supplementary material section under Figure S4.

2.3. Ambipolar charge transfer

To analyze in detail the charging and discharging processes of the C_{84} , we performed nc-AFM measurements on molecular islands. An STM-topography of the investigated C_{84} island is presented in Fig. 3 (a). The nc-AFM images at positive and negative sample bias are shown in Fig. 3 (b) and (c), respectively. We find characteristic discharging rings for positive and negative sample biases [29]. The charging rings appear concentric and have bias-dependent radii. The specific diameter of the (dis-)charging rings, much like the (dis-)charging peak in STS, depends on how close the frontier molecular orbital of the C_{84} undergoing the charge transfer is to Fermi energy, i.e., how much tip electric field is needed for the frontier orbital to cross Fermi energy. We find that 88 % of the superstructure pores covered with C_{84} experience either a discharging or charging event with a ratio of 3:1 between discharging to charging. However, this ratio is dependent on the applied sample bias voltage window. The ratio of 3:1 will decrease when the charging of neutral C_{84} increases once the electric field is raised to a point where the LUMO of neutral C_{84} on the rim of the wire or even on top of the wire start to become accessible to a charge transfer process.

While there appears to be no more than one discharging and one charging event per pore, we find that a charging and discharging process can happen in the same pore. An STM topography and nc-AFM images for positive and negative sample bias of this phenomenon are presented in Fig. 3 (d)–(f), respectively. The two neighboring fullerenes, labeled A and B, show discharging and charging rings at positive and negative sample bias, respectively. The distance of the two charging ring centers is 1.2 nm, matching the typical nearest neighbor distance of the C_{84} in the molecular islands. For the chosen tip position indicated by the blue

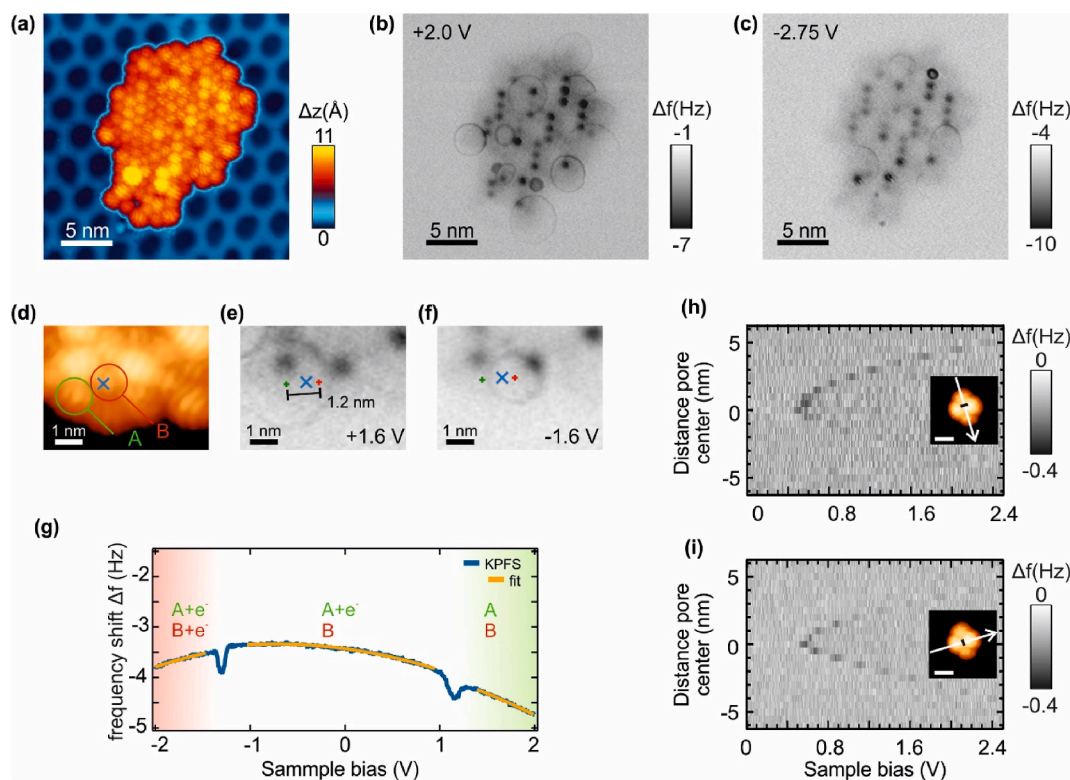


Fig. 3. Characterization of the two charge transfer processes. (a) STM topography of the C_{84} island investigated with nc-AFM in (b) and (c) (setpoint: -1.2 V, 10 pA). (b) nc-AFM image at $+2.0$ V displaying discharging rings (setpoint: 400 pA, excitation amplitude: 50 p.m., Q-factor: $35k$). (c) nc-AFM image at -2.75 V displaying charging rings (setpoint: 400 pA, excitation amplitude: 50 p.m., Q-factor: $35k$). (d) STM topography of a part of the C_{84} island investigated with nc-AFM in (e) and (f) (setpoint: 2 V, 10 pA). Two C_{84} that undergo tip induced charge transfer labeled A (discharging) and B (charging). (e)–(f) nc-AFM at $+1.6$ V, respectively (setpoint: 500 pA, excitation amplitude: 50 p.m., Q-factor: $35k$). (g) KPFS measurement and fit at the position of the blue cross, indicated in (d)–(f) (setpoint: 2 V, 500 pA, excitation amplitude: 50 p.m., Q-factor: $8K$). Areas where both molecules are charged (red), only A charged (white) and both neutral (green). (h)–(i) KPFS point spectra along two directions (white arrows) over a cluster of C_{84} , indicated in the STM topographies in the inset. The background of the KPFS spectra was removed and the dark contrast results from the discharging events that is visible as a dip in original Kelvin parabola (setpoint: 2 V, 500 pA, excitation amplitude: 50 p.m., Q-factor: $8K$, scale bar 2 nm).

cross, both charge transfer processes, i.e., the discharging of intrinsically charged C_{84} (fullerene A) and charging of neutral C_{84} (fullerene B), can be observed as dips in the Kelvin parabola [29,30] in the same KPFS measurement shown in Fig. 3 (g). A full series of KPFS point spectra between the two fullerenes is provided in Figure S5. While the exact voltage of the charge transfer processes depends on the tip position, we find that both processes are accessible in similar bias ranges around ± 1.2 V.

The distance dependency between tip position and charge transfer process is shown via KPFS point spectra along the two directions of a small C_{84} cluster in Fig. 3 (h) and (i). The dips in the Kelvin parabola represent the distance for discharging at a given sample bias, resulting in the expected discharging parabola. The lower arm of the parabola in the measurement in Fig. 3 (h) is hardly visible. From the lack of signal and the position of the parabola's minima, we can identify the C_{84} in the top part of the STM topography to be the one that is intrinsically charged by the substrate and subject to the discharging process.

2.4. Coulomb interaction of charged C_{84}

As we have shown in the previous paragraph, charging processes of the same type occur at most once per single pore. However, neighboring pores' discharging rings can cross for large enough sample biases, as seen in the nc-AFM series with increasing sample bias in Fig. 4 (a). Upon reaching a bias where the rings meet, they appear to repel each other, forming a boundary between them (see panels 1.25 V and 1.5 V in Fig. 4 (a)). Further increasing the sample bias reveals two new segments of discharging rings with reduced radii, one for each fullerene. A

discharging ring of reduced radius means a higher field or applied sample bias is needed to promote the charge transfer process. Therefore, discharging a charged C_{84} becomes easier the higher the number of charged C_{84} in its surroundings due to Coulomb repulsion. A similar phenomenon has already been observed for copper phthalocyanines on h-BN/Cu(111) [30] and for correlated electron systems in back gated WS_2/WS_2 Moiré lattices [31]. Due to the concentric shape of the charging rings, we can calculate the associated energy difference of discharging a fullerene with and without a second charge at the second nearest neighbor position by fitting the charging rings as shown in Fig. 4 (b) for different sample biases.

Fig. 4 (c) shows a schematic representation of the discharging ring interactions of two C_{84} at 1.75 V applied sample bias. As the tip is scanned over the region of the molecules, they can be in different charge states. Solid lines indicate the observed discharging rings. While both fullerenes are charged, the mutual Coulomb repulsion shifts the $L + e^-$ states of both molecules closer to the Fermi energy. This means that the discharging of either C_{84} requires a lower electric field, i.e., STM bias, compared to the case where the nearby C_{84} was charge neutral. To rationalize this, we consider the system of two charged C_{84} , as presented in Fig. 4. We label the state where both C_{84} are negatively charged as $(-1, -1)$. When we move the tip from left to right in the axis of the two molecules, we will first observe a charge transition of the left C_{84} to the neutral state while the right molecule remains charged; we denote this as the state $(0, -1)$. Moving the tip further to the right will also discharge the right C_{84} to the state $(0, 0)$. Next, the left C_{84} becomes negatively charged again to $(-1, 0)$, and ultimately, the right C_{84} becomes negatively charged again, and the pristine $(-1, -1)$ state is reestablished. The

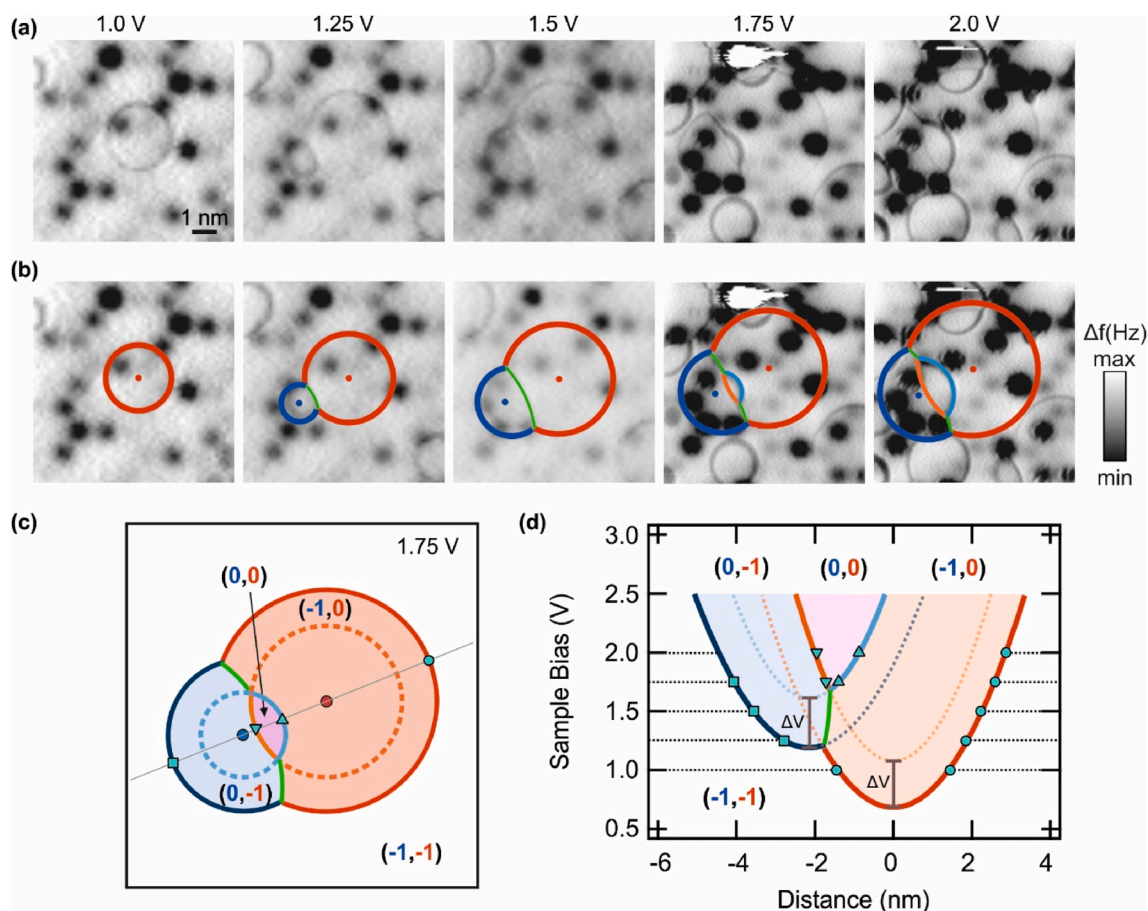


Fig. 4. Interaction between charges. **(a)** nc-AFM series for increasing sample bias from 1 to 2 V. The discharging ring radii increase. Contrast adjusted to increase the visibility of the charging rings. (setpoint: 1000 pA, excitation amplitude: 50 p.m., Q-factor 35K). **(b)** nc-AFM series shown in (a) with color-coded charging rings red for the right and blue for the left fullerene. At 1.5 V the repulsion of the two discharging rings is clearly visible. For biases equal or larger than 1.75 V two new discharging rings emerge highlighted in orange and light blue. **(c)** Schematic of the discharging rings at 1.75 V. Red and blue for interacting and (dotted) orange and light blue for non-interacting C_{84} . The regions for the different charge states where no C_{84} $(-1,-1)$, only the red $(-1,0)$, only the blue $(0,-1)$ or both $(0,0)$ fullerenes are discharged are indicated. **(d)** Discharging parabolas for the two fullerenes in neighboring pores. The parabolas are fits for the radii of the discharging rings (cyan symbols) at different voltages. The additional voltages of 0.4 V needed to discharge a second fullerene are indicated.

solid blue and solid red circles are charging rings associated with the $(-1,-1) \rightarrow (0,-1)$ and the $(-1,-1) \rightarrow (-1,0)$ transitions, respectively. The light blue and orange circle segments denote the $(-1,0) \leftrightarrow (0,0)$ and $(0,-1) \leftrightarrow (0,0)$ transitions, respectively, and are extended to full (hypothetical) charging circles by the dotted lines. There are also $(-1,0) \leftrightarrow (0,-1)$ transition lines marked as solid green lines, where the field is not strong enough to stabilize the fully neutral $(0,0)$ state. The green, orange and light blue line meet in two triple degeneracy points of the $(0,0)$, $(-1,0)$ and $(0,-1)$ states. A very similar behavior was observed in the transport behavior of coupled Quantum Dots (QDs) where the charge of one QD affects the charging and discharging behavior of the neighboring QDs [32].

From this analysis, we can construct the charging paraboloids from the diameter of the charging rings at different applied sample biases. A cut along the line connecting the two fullerenes is shown in Fig. 4 (d). From the parabolas, we can determine the minimal voltage needed to promote the first charge transfer, which is 0.7 V for the orange $(-1,-1) \rightarrow (-1,0)$ and 1.2 V for the blue $(-1,-1) \rightarrow (0,-1)$ for the right and left C_{84} respectively. The double discharge parabolas for the $(-1,0) \rightarrow (0,0)$ and $(0,-1) \rightarrow (0,0)$ transitions in orange and light blue are shifted up in voltage by 0.4 V. From this shift, we can estimate the coulomb repulsion of the two charged C_{84} . With the previously calculated Voltage drop across the molecule of 16.2 %, we can calculate the coulomb energy of 65 meV. The two C_{84} considered here are 2nd nearest neighbors with a distance of about 2.4 nm. I.e., the negative charge of one molecule shifts

the $L + e^-$ of the other closer to the Fermi energy by about 65 meV.

2.5. Perspective on device integration

Our results demonstrate the possibilities to control interface properties regarding charge transfer within the combination of organic and 2D materials. A detailed understanding of how the two materials interact can lead to exciting new properties like the above-presented ambipolar charge transfer for C_{84} on the h-BN/Rh(111) Moiré superstructure. We see a potential application of the material system in the field of nanotechnology, especially for ambipolar FETs. Using only the LUMO orbital as the electron donor and acceptor could have significant advantages over conventional approaches where both HOMO and LUMO are used for charge carrier injection. In a perfectly aligned system, the energy barrier to inject electrons/holes would be half the experimentally obtained HOMO-LUMO gap, so 1.15 ± 0.1 eV. Using the LUMO and the $L + e^-$ instead would reduce the energy barrier for charge carrier injection by a factor of 10 to 0.11 ± 0.05 eV, which in turn could significantly reduce the operation voltages. Usually, the energy level alignment will not be perfect, and there is an imbalance between the energies needed for electron and hole injection. However, we find the energies required to promote the charge transfer for electrons and holes using $L + e^-$ and LUMO around similar energies, making them equally accessible.

One of the biggest challenges in ambipolar FETs is an efficient hole

and electron injection via the electrodes. For a single-channel transistor, ideally, the electrodes' work function aligns with the organic semiconductor's molecular orbital. In the case of ambipolar transistors, at least one type of charge carrier will be limited by the contact [33]. In the presented work, only the LUMO orbital is used for the electron and hole injection. Thus, the work function of the electrode material only needs to be tuned for one molecular orbital. Since the LUMO shifts once it is populated, we find a minimum effective gap between LUMO and $L + e^-$ of 0.22 eV. Consequently, there will still be a slight mismatch. However, it can be expected to be significantly smaller than a conventional organic semiconductor–contact mismatch, which will be in the order of the band gap, usually between 2 and 3 eV.

In addition to the smaller contact mismatch, there are advantages in using the LUMO - $L + e^-$ gap as ambipolar system compared to other small band gap organic semiconductors like acenes or conjugated semiconducting polymers. Lowering the intrinsic HOMO-LUMO gap can lead to an increased reactivity and can decrease the transport properties, both effects adverse for device performance and longevity [34,35].

With the advantages mentioned above, some challenges need to be addressed. Experiments on C_{84} thin film-based FETs found decent carrier mobility ($2.1 \times 10^{-3} \text{ cm}^2 \text{ V}^{-1} \text{ s}^{-1}$) and a hopping n-type transport mechanism [10]. However, as only a portion of the fullerenes is involved in either direction of the presented charge transfer process, it will be crucial to investigate whether the charge carrier density is high enough to allow for a decent charge transport. Additionally, while the required energies for charge transfer are in similar ranges, we find an imbalance in charging vs. discharging of 1:3, which in turn could lead to an imbalance in the charge carrier densities. While our results show no intrinsic charge transfer from the substrate to pure C_{60} , one could use the more conventional fullerene derivatives and achieve the desired energy level alignment by partial electron transfer from an added functional group [36,37].

Concerning the device architecture, it would be beneficial to use only a thin film of Rhodium on a semiconducting substrate [38] to allow for a Moiré pattern to develop while at the same time enabling the gating of the device without the dissipation of the charge carriers into the metal.

A more accessible material combination for a thin film approach could be the h-BN/Ni(111) system. Due to the lattice commensurability of the h-BN and the Ni(111) surface, this system develops an atomically flat surface without a Moiré superstructure. The work function of the h-BN/Ni(111) system (3.55 eV) [39] is very close to the work function of the pore region in the h-BN/Rh(111) system (3.6 eV) [18], which should result in an intrinsic charge transfer from the substrate to the C_{84} . However, as was discussed in the previous chapter, charged fullerenes interact with each other. This interaction should prevent the electron transfer to all C_{84} and result in a charged/uncharged array of C_{84} with a suitable energy level alignment to allow ambipolar charge transfer.

Alternatively, there are different ways to facilitate a Moiré potential without needing a metal substrate, for example, by using twisted bilayers of 2D materials like Silicene [40] or MoS_2 [41]. For small angle twisted bilayer MoS_2 , the potential strength is between 100 and 200 meV, which is between 20 and 40 % of the potential difference found on the h-BN/Rh(111) Moiré. While significantly smaller, the potential difference could be enough to induce intrinsic charge transfer on organic molecules and result in accessible LUMO and $L + e^-$ orbitals to promote ambipolar charge transfer.

3. Conclusion

In summary, we have studied and compared the electronic properties and charge transfer processes of the three fullerenes, C_{60} , C_{70} , and C_{84} . We could experimentally verify the expected shrinking of the HOMO-LUMO gap with increasing fullerene size. For all three fullerenes, we found a dependency of the energy level alignment with respect to the adsorption position on the h-BN/Rh(111) Moiré superstructure. As such, the LUMO of fullerenes adsorbed in the pore of the superstructure is

close enough to fermi energy to observe and induce single electron charge transfer via the field effect using an STM tip. Only for the largest fullerene, the C_{84} , we find an intrinsic charge transfer from the substrate if the C_{84} is adsorbed in the Moiré pore center. In coherence with the charging of the fullerenes, the intrinsically charged C_{84} can be discharged. Here, we could quantify the coulomb interaction between charges by analyzing the crossing of discharging rings. As a result, we induced ambipolar charge transfer on the C_{84} h-BN/Rh(111) system. The combination of the Moiré potential landscape and the field effect of the STM tip facilitates the charge transfer.

In conclusion, the potential applications in nanotechnology, exemplified by an ambipolar FET, are significant. Utilizing a single molecular orbital as both an electron donor and acceptor presents substantial advantages over conventional organic semiconductors in terms of efficiency, charge carrier injection, and balance. While the functionality of the ambipolar charge transfer is demonstrated as a proof of principle, further efforts will be needed to investigate parameters like the charge carrier density in an actual device geometry.

4. Experimental methods

4.1. Sample preparation

A UHV preparation chamber with a base pressure in the mid 10-10 mbar range was utilized to carry out the different stages of sample preparation. Initially, the Rh(111) single crystal surface underwent cleaning via recurrent cycles of Ar^+ sputtering and annealing, conducted at 850 °C. During sputtering, the temperature of the crystal was maintained at 500 °C to prevent argon inclusions. Subsequently, the growth of the h-BN monolayer was achieved by decomposing borazine (HBNH_3) gas at 2×10^{-7} mbar for 10 min on the 800 °C hot Rh(111) surface. The borazine source was degassed by performing three freeze-pump cycles before dosing the gas into the preparation chamber. After decomposition, the crystal was annealed for 2 min and cooled gradually to prevent defect formation.

Three different fullerenes were used in the experiments: C_{60} (Sigma Aldrich), 99.95 % pure, C_{70} synthesized by Konstantin Amsharov, and C_{84} (ABCR), 95 % pure. The fullerenes C_{60} , C_{70} , and C_{84} were sublimated from a quartz crucible onto the crystal surface at 430 °C, 580 °C, and 610 °C, respectively. The Rh(111) surface was kept at approximately 100 °C during all fullerene sublimations to facilitate fullerene island formation.

4.2. Measurements

Scanning probe measurements were performed in a commercial Omicron scanning probe microscope with Q + AFM. Experiments were conducted at a temperature of 4.5 K and UHV conditions with a base pressure in the low 10^{-10} mbar range. An 80:20 Pt:Ir tip attached to a commercial Q+ tuning fork with a resonance frequency of 24.7 kHz was used for STM, STS, nc-AFM, and KPFS measurements. Tip forming was performed before the experiments on a clean Au(111) single crystal.

The STM images were captured using the constant current mode with specified setpoint values, as mentioned in the caption of the figures. The dI/dV spectra were gathered utilizing the lock-in technique in the constant height mode with the setpoint values indicated in the captions of the figures.

The KPFS spectra and nc-AFM images were recorded in the constant height mode, measuring the frequency shift of a Pt:Ir tip connected to a Q+ sensor via Omicron Matrix Electronics and a Zurich Instruments HF2Li PLL. The excitation amplitude, Q-factor, and setpoint values are indicated in the captions.

4.3. Data analysis

The presented data were processed with Wave Metrics Igor Pro 8.

4.4. DFT calculations

The DFT calculations were performed using an AiiDalab [42] application based on AiiDa workflows [43] for the Gaussian code [44]. We used B3LYP as an approximation of the exchange-correlation functional [45,46]. The atomic positions of the C₈₄ molecules were optimized for the different charge states. We used a 6–311** basis set to represent the Kohn-Sham orbitals.

CRediT authorship contribution statement

Max Bommert: Investigation, Validation, Formal analysis, Data curation, Writing – original draft, Visualization. **Bruno Schuler:** Investigation, Writing – review & editing. **Carlo A. Pignedoli:** Investigation, Formal analysis, Data curation, Writing – review & editing. **Roland Widmer:** Investigation, Writing – review & editing. **Oliver Gröning:** Conceptualization, Supervision, Formal analysis, Resources, Writing – review & editing, Funding acquisition.

Declaration of competing interest

The authors declare that they have no known competing financial interests or personal relationships that could have appeared to influence the work reported in this paper.

Acknowledgments

This research was funded by the Swiss National Science Foundation under Grant No. 200021_165512 and the NCCR MARVEL, funded by the Swiss National Science Foundation under Grant No. 51NF40-182892. B. S. appreciates funding from the European Research Council (ERC) under the European Union's Horizon 2020 research and innovation program (Grant Agreement No. 948243). We acknowledge a grant from the Swiss National Supercomputing Centre (CSCS) under project ID s1141for computational resources. We acknowledge PRACE for awarding access to the Fenix Infrastructure resources at CSCS, which is partially funded by the European Union's Horizon 2020 research and innovation program through the ICEI project under grant agreement No. 800858.

The authors want to thank Konstantin Amsharov for providing the C₇₀ molecules. In addition, the authors thank Lukas Rotach for his outstanding technical support during the experiments.

For the purpose of Open Access, the author has applied a CC BY public copyright license to any Author Accepted Manuscript version arising from this submission.

Appendix A. Supplementary data

Supplementary data to this article can be found online at <https://doi.org/10.1016/j.carbon.2023.118592>.

References

- [1] D. Jariwala, S.L. Howell, K.-S. Chen, J. Kang, V.K. Sangwan, S.A. Filippone, R. Turrissi, T.J. Marks, L.J. Lauhon, M.C. Hersam, *Nano Lett.* 16 (2016) 497.
- [2] H.G. Ji, P. Solís-Fernández, D. Yoshimura, M. Maruyama, T. Endo, Y. Miyata, S. Okada, H. Ago, *Adv. Mater.* 31 (2019), 1903613.
- [3] J. Liu, K. Zhou, J. Liu, J. Zhu, Y. Zhen, H. Dong, W. Hu, *Adv. Mater.* 30 (2018), 1803655.
- [4] J.-Y. Seo, J. Choi, H.-S. Kim, J. Kim, J.-M. Yang, C. Cuhadar, J. Su Han, S.-J. Kim, D. Lee, H. Won Jang, N.-G. Park, *Nanoscale* 9 (2017), 15278.
- [5] P. Xiong, Y. Wu, Y. Liu, R. Ma, T. Sasaki, X. Wang, J. Zhu, *Energy Environ. Sci.* 13 (2020) 4834.
- [6] W.H. Lee, J. Park, S.H. Sim, S.B. Jo, K.S. Kim, B.H. Hong, K. Cho, *Adv. Mater.* 23 (2011) 1752.
- [7] T. Xu, S. Fan, M. Cao, T. Liu, J. Su, *Appl. Phys. Lett.* 120 (2022), 073301.
- [8] S. Kobayashi, T. Takenobu, S. Mori, A. Fujiwara, Y. Iwasa, *Appl. Phys. Lett.* 82 (2003) 4581.
- [9] T. He, C.D. Frisbie, *ACS Nano* 16 (2022) 4823.
- [10] K. Shibata, Y. Kubozono, T. Kanbara, T. Hosokawa, A. Fujiwara, Y. Ito, H. Shinohara, *Appl. Phys. Lett.* 84 (2004) 2572.
- [11] Y. Ren, X. Yang, L. Zhou, J.-Y. Mao, S.-T. Han, Y. Zhou, *Adv. Funct. Mater.* 29 (2019), 1902105.
- [12] T.D. Anthopoulos, F.B. Kooistra, H.J. Wondergem, D. Kronholm, J.C. Hummelen, D.M. de Leeuw, *Adv. Mater.* 18 (2006) 1679.
- [13] Y. Kunugi, K. Takimiya, N. Negishi, T. Otsubo, Y. Aso, *J. Mater. Chem.* 14 (2004) 2840.
- [14] T. Shimada, T. Okazaki, R. Taniguchi, T. Sugai, H. Shinohara, K. Suenaga, Y. Ohno, S. Mizuno, S. Kishimoto, T. Mizutani, *Appl. Phys. Lett.* 81 (2002) 4067.
- [15] D. Mahdaoui, C. Hirata, K. Nagaoka, K. Miyazawa, K. Fujii, T. Ando, M. Abderrabba, O. Ito, M. Takagi, T. Ishimoto, M. Tachikawa, S. Yagyu, Y. Liu, Y. Nakajima, Y. Nemoto, K. Tsukagoshi, T. Wakahara, *J. Mater. Chem. C* 10 (2022) 3770.
- [16] C.R. Dean, A.F. Young, I. Meric, C. Lee, L. Wang, S. Sorgenfrei, K. Watanabe, T. Taniguchi, P. Kim, K.L. Shepard, J. Hone, *Nat. Nanotechnol.* 5 (2010) 722.
- [17] K. Zhang, Y. Feng, F. Wang, Z. Yang, J. Wang, *J. Mater. Chem. C* 5 (2017), 11992.
- [18] H. Dil, J. Lobo-Checa, R. Laskowski, P. Blaha, S. Berner, J. Osterwalder, T. Greber, *Science* 319 (2008) 1824.
- [19] L. Liu, T. Dienel, R. Widmer, O. Gröning, *ACS Nano* 9 (2015), 10125.
- [20] M. Bommert, G. Günzburger, R. Widmer, B. Schuler, O. Gröning, *Adv. Phys. Res.* 2 (2023), 2300029.
- [21] Y. Yang, F. Arias, L. Echegoyen, L.P.F. Chibante, S. Flanagan, A. Robertson, L. J. Wilson, *J. Am. Chem. Soc.* 117 (1995) 7801.
- [22] S. Berner, M. Corso, R. Widmer, O. Groening, R. Laskowski, P. Blaha, K. Schwarz, A. Goriachko, H. Over, S. Gsell, M. Schreck, H. Sachdev, T. Greber, *J. Osterwalder, Angew. Chem. Int. Ed.* 46 (2007) 5115.
- [23] M. Corso, W. Auwärter, M. Muntwiler, A. Tamai, T. Greber, *J. Osterwalder, Science* 303 (2004) 217.
- [24] Y. Ding, M. Iannuzzi, J. Hutter, *J. Phys. Chem. C* 115 (2011), 13685.
- [25] R. Kuzuo, M. Terauchi, M. Tanaka, Y. Saito, H. Shinohara, *Phys. Rev. B* 49 (1994) 5054.
- [26] Z. Rostami, A. Hosseini, A. Monfared, *J. Mol. Graph. Model.* 81 (2018) 60.
- [27] G. Sun, M. Kertesz, *J. Phys. Chem. A* 105 (2001) 5212.
- [28] H. Liang, S. Xu, W. Liu, Y. Sun, X. Liu, X. Zheng, S. Li, Q. Zhang, Z. Zhu, X. Zhang, C. Dong, C. Li, G. Yuan, H. Mimura, *Phys. Lett.* 377 (2013) 2676.
- [29] N. Kocić, P. Weiderer, S. Keller, S. Decurtins, S.-X. Liu, J. Repp, *Nano Lett.* 15 (2015) 4406.
- [30] M. Pörtner, Y. Wei, A. Riss, K. Seufert, M. Garnica, J.V. Barth, A.P. Seitsonen, L. Diekhöner, W. Auwärter, *Adv. Mater. Interfaces* 7 (2020), 2000080.
- [31] H. Li, S. Li, M.H. Naik, J. Xie, X. Li, E. Regan, D. Wang, W. Zhao, K. Yumigeta, M. Blei, T. Taniguchi, K. Watanabe, S. Tongay, A. Zettl, S.G. Louie, M.F. Crommie, *F. Wang, Nat. Phys.* 17 (2021) 1114.
- [32] M. Seo, H.K. Choi, S.-Y. Lee, N. Kim, Y. Chung, H.-S. Sim, V. Umansky, D. Mahalu, *Phys. Rev. Lett.* 110 (2013), 046803.
- [33] J. Zausseil, H. Sirringhaus, *Chem. Rev.* 107 (2007) 1296.
- [34] C. Tönshoff, H.F. Bettinger, *Chem. Eur. J.* 27 (2021) 3193.
- [35] M.C. Scharber, N.S. Sariciftci, *Adv. Mater. Technol.* 6 (2021), 2000857.
- [36] Y. Itoh, B. Kim, R.I. Gearba, N.J. Tremblay, R. Pindak, Y. Matsuo, E. Nakamura, C. Nuckolls, *Chem. Mater.* 23 (2011) 970.
- [37] C. Yang, S. Cho, A.J. Heeger, F. Wudl, *Angew. Chem. Int. Ed.* 48 (2009) 1592.
- [38] F. Müller, S. Hüfner, H. Sachdev, *Surf. Sci.* 603 (2009) 425.
- [39] M. Schaal, T. Aihara, M. Gruenewald, F. Otto, J. Domke, R. Forker, H. Yoshida, T. Fritz, *Beilstein J. Nanotechnol.* 11 (2020) 1168.
- [40] M. Zhao, J. Zhuang, Q. Cheng, W. Hao, Y. Du, *Small* 17 (2021), 1903769.
- [41] N. Tilak, G. Li, T. Taniguchi, K. Watanabe, E.Y. Andrei, *Nano Lett.* 23 (2023) 73.
- [42] A.V. Yakutovich, K. Eimre, O. Schütt, L. Talirz, C.S. Adorf, C.W. Andersen, E. Dittler, D. Du, D. Passerone, B. Smit, N. Marzari, G. Pizzi, C.A. Pignedoli, *Comput. Mater. Sci.* 188 (2021), 110165.
- [43] G. Pizzi, A. Cepellotti, R. Sabatini, N. Marzari, B. Kozinsky, *Comput. Mater. Sci.* 111 (2016) 218.
- [44] Gaussian 16, Revision C.01 M.J. Frisch, G.W. Trucks, H.B. Schlegel, G.E. Scuseria, M.A. Robb, J.R. Cheeseman, G. Scalmani, V. Barone, G.A. Petersson, H. Nakatsuji, X. Li, M. Caricato, A.V. Marenich, J. Bloino, B.G. Janesko, R. Gomperts, B. Mennucci, H.P. Hratchian, J.V. Ortiz, A.F. Izmaylov, J.L. Sonnenberg, D. Williams-Young, F. Ding, F. Lipparini, F. Egidi, J. Goings, B. Peng, A. Petrone, T. Henderson, D. Ranasinghe, V.G. Zakrzewski, J. Gao, N. Rega, G. Zheng, W. Liang, M. Hada, M. Ehara, K. Toyota, R. Fukuda, J. Hasegawa, M. Ishida, T. Nakajima, Y. Honda, O. Kitao, H. Nakai, T. Vreven, K. Throssell, J. A. Montgomery Jr., J.E. Peralta, F. Ogliaro, M.J. Bearpark, J.J. Heyd, E. N. Brothers, K.N. Kudin, V.N. Staroverov, T.A. Keith, R. Kobayashi, J. Normand, K. Raghavachari, A.P. Rendell, J.C. Burant, S.S. Iyengar, J. Tomasi, M. Cossi, J. M. Millam, M. Klene, C. Adamo, R. Cammi, J.W. Ochterski, R.L. Martin, K. Morokuma, O. Parkas, J.B. Foresman, D.J. Fox, Gaussian, Inc., Wallingford CT, 2016.
- [45] C. Lee, W. Yang, R.G. Parr, *Phys. Rev. B* 37 (1988) 785.
- [46] A.D. Becke, *J. Chem. Phys.* 98 (1993) 5648.